ELSEVIER

Contents lists available at ScienceDirect

International Journal of Refractory Metals and Hard Materials

journal homepage: www.elsevier.com/locate/IJRMHM



Residual elastic strain evolution due to thermal cycling of a ceramic-metal composite (WC-Cu) via high energy X-ray diffraction and analytical modeling

John I. Ferguson^a, Armand J. Beaudoin^b, Gregory D. Scofield^c, J.Y. Peter Ko^b, Kelly E. Nygren^b, Yujie Wang^c, Mario Caccia^c, Kenneth H. Sandhage^c, Michael D. Sangid^{a,c,*}

ARTICLE INFO

Keywords: Ceramic-metal composites Stress relaxation Residual stress Kinetics modeling

ABSTRACT

Residual stress, when superimposed with in-service loading, can significantly reduce the lifetime and performance of a component. Ceramic-metal composites are susceptible to residual stresses due to the thermal expansion mismatch of the ceramic and metallic phases. The WC-Cu composite explored in the present study provides a promising combination of thermal conductivity and strength properties, while exhibiting counterintuitive improvements in strength and ductility after thermal cycling. This work quantifies the evolution of the residual elastic strains as a result of processing and cyclic thermal loading in a co-continuous WC-Cu composite through experimental high energy X-ray diffraction and kinetics-based modeling. Both analyses indicate that processing-induced residual tensile stress in the copper phase is relieved upon subsequent thermal cycling, with kinetics modeling revealing the cyclic-dependent nature of the active power-law creep mechanisms. The results indicate that, through stress relaxation, this material system maintains structural stability during thermal cycling. The illustrated kinetics of relaxation can inform general material processors and designers of ceramicmetal composites to minimize detrimental residual stress and improve performance of these material systems.

1. Introduction

Ceramic-metal composites (cermets) can provide an appealing combination of properties that are unattainable by monolithic ceramics or metals. The goal of these material systems is generally to leverage the beneficial hardness, strength-to-weight ratio, and high temperature behavior of the ceramic phase, while maintaining macro-scale ductility and damage tolerance via incorporation of the metallic phase. Specifically, a cermet comprised of tungsten carbide (WC) and copper (Cu) combines the extreme hardness and strength retention at elevated temperatures of WC with the high ductility and thermal conductivity of Cu. Excellent wetting of liquid Cu with WC has been reported [1], with WC-Cu composites exhibiting good interfacial strength [2]. Potential applications for a WC-Cu cermet include concentrated solar power components [3], tooling for machining processes [4], and fusion divertor thermal barrier interlayers [5,6].

For composites in which the constituent phases exhibit dissimilar

thermal expansion coefficients, as is common in cermets, elastic incompatibility develops during thermal events, which can result in residual stresses. These residual stresses, especially if tensile in the metallic phase, can be detrimental to strength and lifetime of the materials in application. Due to interest in the application of cemented carbides, several modeling and experimental studies have focused on residual stresses formed in WC-based cermets with primarily nickel (Ni) or cobalt (Co) binders [7–11]. Two- and three-dimensional finite element models have shown bulk tension in the metallic binder phase equilibrated with compression in the WC [7], which is largely dependent on the WC phase morphology [8]. Additionally, several experimental neutron and X-ray diffraction studies have revealed significant processing-induced residual stress in WC-Ni [9] and WC-Co [10] composites, as well as plasticity within the metallic binder phase induced by thermal loading [11].

Metal phase plasticity as a relaxation mechanism of thermal mismatch stress in cermets has been documented in several studies,

^a School of Aeronautics and Astronautics, Purdue University, 701 W. Stadium Ave., West Lafayette, IN 47907, USA

^b Materials Solutions Network at CHESS (MSN-C), Cornell University, 161 Synchrotron Drive, Ithaca, NY 14853, USA

^c School of Materials Engineering, Purdue University, West Lafayette, IN 47907, USA

^{*} Corresponding author at: School of Aeronautics and Astronautics, Purdue University, 701 W. Stadium Ave., West Lafayette, IN 47907, USA. *E-mail address:* msangid@purdue.edu (M.D. Sangid).

typically for cermets containing ~ 10 wt% of the metal phase; however, such modeling activities have focused on the viscoplastic behavior [12,13], without the incorporation of time-dependent kinetic relationships. Additionally, prior work in residual stress analyses of cermets has focused on cemented carbides, with microstructural, phase composition, phase content, and fabrication differences compared to the present study. These factors as well as defect kinetic behavior are expected to significantly influence the stress state of the WC-Cu cermet studied in this work. Therefore, the purpose of this paper is to characterize the residual elastic strain state of a melt-infiltrated, co-continuous WC(43 vol%)-Cu composite exposed to various thermal cycles and to rationalize this behavior via the kinetics of the Cu stress relaxation.

2. Material and methods

The WC-Cu composite was fabricated via melt infiltration of a porous WC preform. A WC/binder powder mixture, with an initial WC particle size range of 8.5 to 11.5 μm, was cold pressed into a plate shape (3.5 cm imes 3.5 cm imes 5.5 mm) and then partially sintered for 2 h at 1400 °C (to induce necking between adjacent WC particles for enhanced rigidity). The WC plate was then infiltrated with liquid Cu at 1200 °C, followed by cooling to room temperature at 15 °C/min, to yield a co-continuous composite comprised of 43 vol% WC and 57 vol% Cu. Afterwards, the WC particles remained spherical, based on scanning electron microscope (SEM) observations about two orthogonal planes. To explore the thermal stability of this material, samples were subjected to three different thermal cycles, as well as a baseline (as processed or Uncycled) condition. Heat treatments of the composite plates were conducted to (i) 550 °C at a 15 °C/min rate for one cycle (1× Cycled) with a 5-min dwell at the peak temperature, (ii) 550 °C at a 15 °C/min rate for ten cycles (10× Cycled) with a 5-min dwell at the peak temperature, and (iii) $550\,^{\circ}\text{C}$ at a 15 $^{\circ}\text{C/min}$ rate for one cycle (Annealed) with a 50-min dwell at the peak temperature. Specimens for flexure testing were cut from each plate by electrical discharge machining (EDM), followed by surface grinding with edge chamfering, to yield bars with dimensions of 2 mm \times 1.5 mm \times 25 mm. Specimens for X-ray characterization were also cut from the plates by EDM to produce bars with dimensions of 3 mm \times 3 mm × 10 mm, followed by surface polishing with 800 grit sandpaper to minimize any effect of the EDM on the residual elastic strain measurements.

Four-point flexural tests were conducted at room temperature in accordance with ASTM C1161–18. Such tests were conducted on ten asinfiltrated specimens (Uncycled) and ten post-infiltration heat-treated specimens to 550 °C with a 5-min dwell for ten cycles (10× Cycled). For microstructural characterization, specimens were cross-sectioned, then mechanically polished to a 1 μm diamond finish followed by a final 24 h vibratory polish with colloidal silica media (20–40 nm particle size). Electron backscatter diffraction (EBSD) was conducted on specimens using a FEI Quanta 650 SEM with an EDAX EBSD Camera. The EBSD scans were conducted with a 10 kV beam voltage and a 5 spot size with a step size of 500 nm. Data processing was performed with the EDAX OIM Analysis software.

Elastic strain measurements were performed on the Structural Materials Beamline (SMB) at the Cornell High Energy Synchrotron Source (CHESS). Energy Dispersive X-ray Diffraction (EDD), while commonly used for determining spatial fields of residual elastic strain across a sample or component, was selected as the experimental mode due to the high atomic number of WC, requiring high energies for X-ray transmission, and to identify the residual elastic strain of each phase in a single region, simultaneously, by post-processing the diffraction peak profiles corresponding to each crystal structure. EDD was employed with polychromatic X-rays (50–200 keV) and a single-element Canberra GL-0055 energy-resolved detector positioned downstream of the sample at a horizontal takeoff angle (2 θ) of 6.05596°. The EDD technique employs a transmission mode of X-ray diffraction. The diffraction volume, or sampling region, was defined by both the upstream slit (0.150 mm

width by 1 mm height) and the downstream detector slits (0.150 mm width by 1 mm height) to produce a diffraction volume lozenge of 2.84 mm length along the cross-section of the specimen. The samples were mounted with the vertical direction perpendicular to the diffraction vector, with the diffraction volume positioned at the mid-length and mid-thickness and rotated along the length axis ($\omega = \pm 90^{\circ}$ at increments of $\Delta\omega = 0.1^{\circ}$ and 5°) to probe a full range of crystalline lattice planes. The EDD analysis was performed using a CHESS software package, consistent with analyses of previous studies [14], which was written in SciPy [15] using modules from HEXRD [16]. The true elastic strains, $\varepsilon_i^{el} = ln(\frac{d^i}{d^i})$, for both phases were calculated via the energy shift of the fitted diffraction peaks, simplified via Bragg's Law for a single takeoff angle as $\varepsilon_i^{el} = ln(\frac{E_0^i}{E^i})$ [17], where, d^i (Å) is the inter-atomic spacing for a specific (i^{th}) lattice plane of the phase in the stressed condition, and d_0^i (Å) is the corresponding stress-free spacing of the same lattice plane, while E^{i} (keV) is the diffracted energy peak of a specific (i^{th}) lattice plane of the phase as determined by the center of the Gaussian curve fit, and E_{α}^{i} (keV) is the corresponding stress-free energy of the same lattice plane. The stress-free lattice parameters for the hexagonal (hP2) WC were determined by performing EDD on the raw WC in original powder form, which were $a_{WC} = 2.906$ Å and $c_{WC} = 2.836$ Å. Additionally, the stressfree lattice parameter for the cubic Cu was acquired from literature, a_{Cu} = 3.615 Å [18], and validated via an EDD measurement of approximately zero residual elastic strain at the free surface of the Annealed sample.

3. Kinetics modeling

A temperature- and time-dependent analytical model, developed by Shen and Suresh for metal-ceramic multilayered materials [19] and implemented by Hoffman et al. in an Al/Al₂O₃ cermet [20], was used to analyze the stress evolution of the Cu phase during process cooling and subsequent heat treatments. In this approach, both phases are assumed to be isotropic ($K = \frac{2G(1+\nu)}{3(1-2\nu)}$), and the homogenized bulk material properties are derived by the effective medium approximation, assuming that each phase is surrounded by a matrix of a random collection of both phases [21]. The elastic properties of both phases are governed by the bulk modulus (K), shear modulus (G), and Poisson factor (ν). The WC is assumed to behave elastically, with the total strain (ε_{WC}) equivalent to the thermal strain (ε_{WC}^T) calculated from the coefficient of thermal expansion (CTE) ($\varepsilon_{WC} = \varepsilon_{WC}^T$). The temperature-dependent CTEs of WC and Cu were digitized from literature values [22,23] and fit with interpolant functions. The CTEs at 25 $^{\circ}$ C and 550 $^{\circ}$ C are: for WC – 4.4 and 5.6 ppm/°C, respectively, and for Cu - 16.7 and 20.0 ppm/°C, respectively. A full list of material properties for both phases is listed in Tables A.1 and A.2 of the Appendix.

This approach leverages kinetics-based plasticity and creep equations to derive the relaxation of the metallic phase to maintain equilibrium and stain compatibility within the overall composite. The total strain (ε_{Cu}) of the Cu phase is the summation of the thermal strain (ε_{Cu}^T), calculated from the temperature dependent CTE, and the relaxation (plastic) strain (ε_{Cu}^{T}) as seen in Eq. 1.

$$\varepsilon_{Cu} = \varepsilon_{Cu}^T + \varepsilon_{Cu}^{rlx} \tag{1}$$

The net relaxation strain rate ($\dot{\epsilon}_{Cll}^{Tx}$) in the Cu phase, quantified as the summation of plasticity (dislocation glide $-\dot{\epsilon}_{dg}$) and identified creep mechanisms (power-law $-\dot{\epsilon}_{pl}$, power-law breakdown $-\dot{\epsilon}_{plb}$, diffusional flow $-\dot{\epsilon}_{diff}$, and Harper-Dorn $-\dot{\epsilon}_{HD}$) as a function of temperature and stress, is found via Eq. 2, as presented by Frost and Ashby [24]. A full description of the individual strain rate equations is listed in Table A.3 of the Appendix.

$$\dot{\varepsilon}_{Cu}^{rlx} = max(\dot{\varepsilon}_{dg}, \dot{\varepsilon}_{pl}, \ or \ \dot{\varepsilon}_{plb}) + max(\dot{\varepsilon}_{diff} \ or \ \dot{\varepsilon}_{HD})$$
(2)

Via equilibrium expressions, the stress in the Cu (σ_{Cu}) can be calculated using the differences in strain between the phases according to Eq. 3 [20]:

$$\sigma_{Cu} = \frac{-3}{V_{Cu}} \frac{K_{Cu}K_{WC}}{K_{Cu} - K_{WC}} \frac{\frac{1}{K^{-}} - \frac{1}{K^{*}}}{\frac{1}{K_{Cu}} - \frac{1}{K_{WC}}} [\varepsilon_{Cu} - \varepsilon_{WC}]$$
(3)

where K^* is the effective bulk modulus and K^- is the inverse rule of mixtures bulk modulus as defined by Kreher and Pompe [21]. Further, V_{Cu} and V_{WC} are the volume fractions of the Cu and WC phases, respectively, of the macroscopic composite. Finally, the bulk stress (σ_{WC}) in the WC can be determined as $\sigma_{WC} = \frac{V_{Cu}}{V_{WC}} \sigma_{Cu}$.

Initializing from the melt temperature of Cu (1085 °C) at an assumed stress-free condition, the model was numerically integrated to identify the relaxation strain of the Cu phase from Eq. 2, for each temperature and time profile of the specimens used in the experiment. Specifically, a constant heating and cooling rate of 15 °C/min was used for cooling from 1200 °C to 25 °C (Uncycled), then three independent thermal treatments were applied from room temperature: (i) one cycle (1× Cycled) to 550 °C with a 5-min dwell at the peak temperature, (ii) ten cycles (10× Cycled) to 550 °C with a 5-min dwell at the peak temperature, and (iii) one cycle (Annealed) to 550 °C with a 50-min dwell at the peak temperature.

4. Results and discussion

Fig. 1 shows the flexure stress versus displacement for all ten specimens of both the as-infiltrated (Uncycled) type and ten-timesthermally-cycled ($10\times$ Cycled) type. The average failure strengths were found to be 957 MPa with a standard deviation of 168 MPa and 1079 MPa with a standard deviation of 92 MPa for the Uncycled and 10× Cycled specimens, respectively. The larger value of mean failure strength for the 10× Cycled specimens relative to the Uncycled specimens was statistically significant within a 95% confidence (p = 0.0297). Such strength retention after thermal cycling indicated that the composite maintained structural stability to 550 °C regardless of the exceptional thermal expansion mismatch ($\alpha_{Cu} = 16 \text{ ppm/}^{\circ}\text{C}$, $\alpha_{WC} = 4$ ppm/°C at room temperature) [22,23]. On average, the elongation to failure of the cycled samples was larger than the uncycled samples, with 4 of 10 cycled samples displaced to the full stroke of the fixture (indicated by star symbols in Fig. 1). The increased room temperature ductility is hypothesized to be a consequence of the elastic residual strain relief during heat treatment, due to stress relaxation up to and at the elevated peak temperature. The more surprising result was the increased failure strength of the cycled sample, which is hypothesized to be due to the increased ductility and negligible increase in the Cu residual stress during cycling to 550 °C due to the mismatch thermal strains and complex constraining of the co-continuous microstructure.

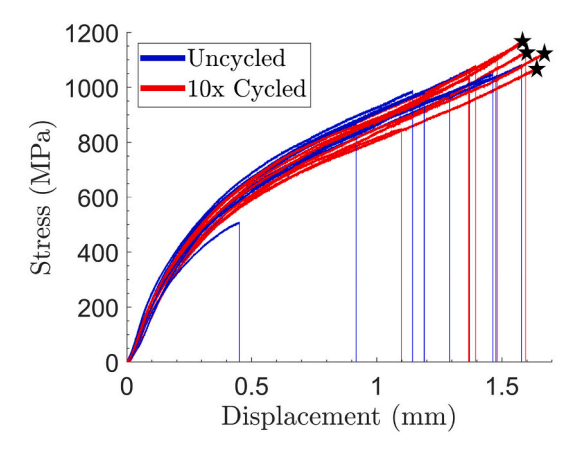


Fig. 1. Room temperature four-point bend flexural tests.

The EDD characterization and kinetics modeling efforts were designed to substantiate these statements.

Figs. 2a and b show the diffracted spectra of both phases in the region of interest from EDD. Coarse rotations (Fig. 2a) of all specimens revealed consistent Bragg diffraction peaks along the WC lattice planes; however, the diffraction peaks of the Cu lattice planes were seldom present. A fine rotation scan (Fig. 2b) about the single previously-identified peak corresponding to the Cu [131] lattice plane revealed an intense peak, which indicated a preferential single orientation texture, satisfying the Bragg condition, in the diffraction volume. EBSD results of the $10\times$ Cycled sample in Fig. 2d confirmed the single orientation throughout the Cu phase. The preferred orientation of Cu was consistent with directional cooling through the samples after melt infiltration. A qualitative view of the intragranular misorientation in the Cu from the EBSD scan was indicative of plasticity that can occur during solidification and/or thermal cycling. From Fig. 2c, the WC phase exhibited nominally random texture and interpenetrating morphology generated during partial sintering at 1400 °C.

The kinetics of stress relaxation of the Cu phase were explicitly modeled for each temperature and time profile, mentioned in Section 3, with the resulting dominant relaxation mechanisms (Eq. 2) active at each temperature shown in Fig. 3a. Upon cooling from infiltration, a transition from high temperature diffusional mechanisms to dislocation dominated power-law creep was observed. The diffusional mechanisms, characterized by Nabarro-Herring type lattice diffusion of atoms, were active from solidification to 700 °C during the low stress, high temperature regime of cooling. A gradual transition occurred at moderate temperatures (700-900 °C) as the diffusional behavior was limited by reduced temperature and the thermal stress began to activate dislocation mechanisms. Below 700 °C, as the internal stresses induced via thermal expansion mismatch increased, power-law creep, characterized by a combination of dislocation climb- and glide-controlled plastic flow, dominated the relaxation. The results indicated that post-process heat treatments resulted in relaxation of the stress in the Cu phase. Fig. 3b illustrates the equilibration of tensile residual stress in the Cu at room temperature after cycling, with repetitive thermal treatments to 550 °C for a 5-min dwell. The reduction of tensile stresses in the Cu phase during thermal cycling was caused by relaxation from previous cycles resulting via iterative reheating to activate the power-law creep mediated relaxation mechanism. Finally, Fig. 3(c-d) reveals the insensitivity of the Cu relaxation on dwell time at 550 °C due to the power-law breakdown creep relaxation strain rate reducing by an order of magnitude at the dwell temperature. The residual tensile stress in the Cu at room temperature was reduced by compressive thermal stress on the Cu upon re-heating. Consequently, the model indicated that the single cycle 5-min dwell (1× Cycled) and 50-min dwell (Annealed) specimens should have nearly identical stress relaxation values in the Cu phase.

The preferentially-oriented Cu throughout the bulk specimens resulted in only a few highly intense diffracted peaks for calculation of the residual elastic strain from the EDD experiment. Consequently, the results were confined to comparisons between the elastic strain calculated from a single diffraction peak. Fig. 4a shows a clear indication of the tensile residual elastic strain in the Cu, relaxed via cycling with direct indications along the [131] and [222] lattice planes. Anisotropy in the elastic strain field was observed in the variation of elastic strain across the lattice planes in the $10\times$ Cycled sample. While outside the scope of this work, the Cu phase could be modeled as a single crystal to capture this anisotropy due to the preferential orientation visualized in Fig. 2d. Fig. 4b indicates similar relaxation trends from the Cu bulk stress in the model (Eq. 3) compared to the X-ray elastic strains.

The randomly-oriented bulk WC phase resulted in detectable lattice plane diffraction peaks for each omega position throughout the EDD scans. From this, the elastic strain in the vertical direction of each sample was determined by the least squares fit of three lattice strains along all rotation angles. From this methodology to experimentally calculate the elastic strains, the results were consistent with the stress

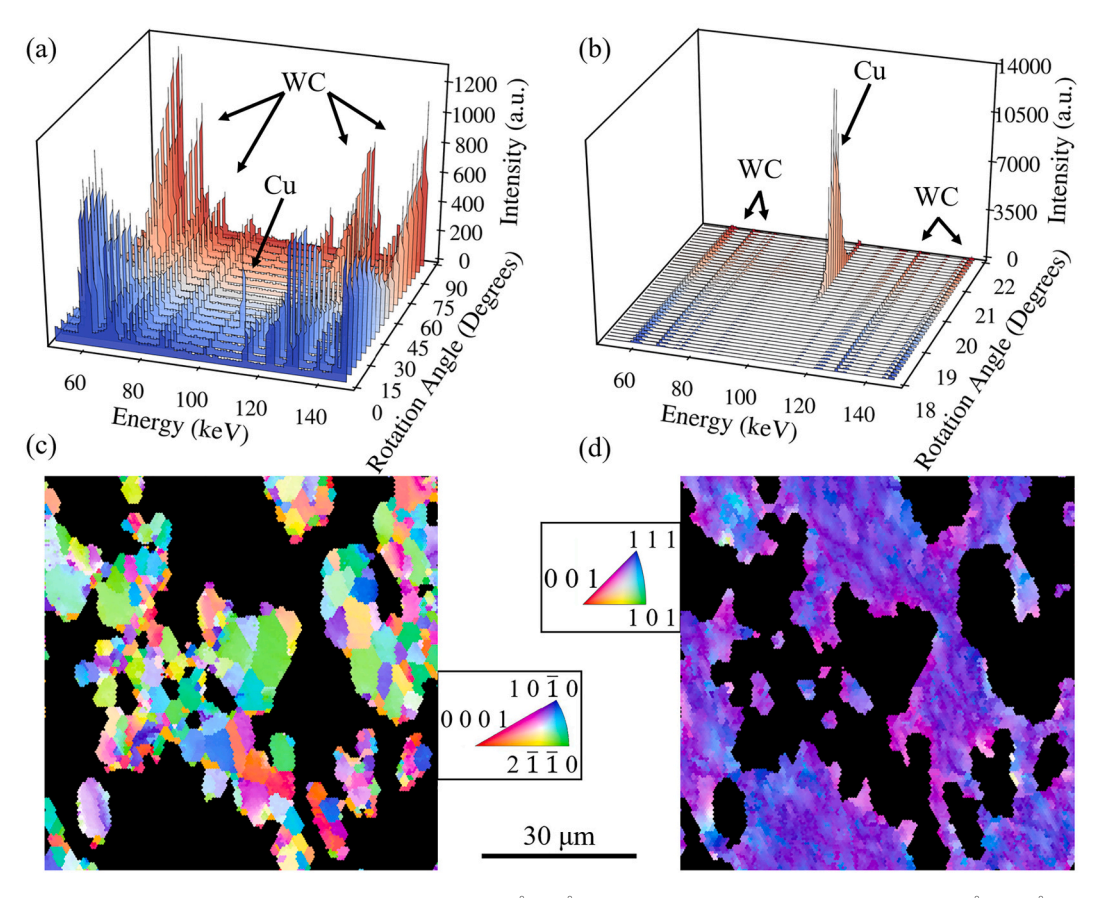


Fig. 2. Full spectra, raw diffraction signal for (a) coarse rotation ($\omega = 0$ –90 $^{\circ}$ at 5 $^{\circ}$ increments) and (b) fine rotation ($\omega = 18$ –22 $^{\circ}$ at 0.1 $^{\circ}$ increments). EBSD IPF orientation map of (c) WC and (d) Cu from the 10× Cycled specimen.

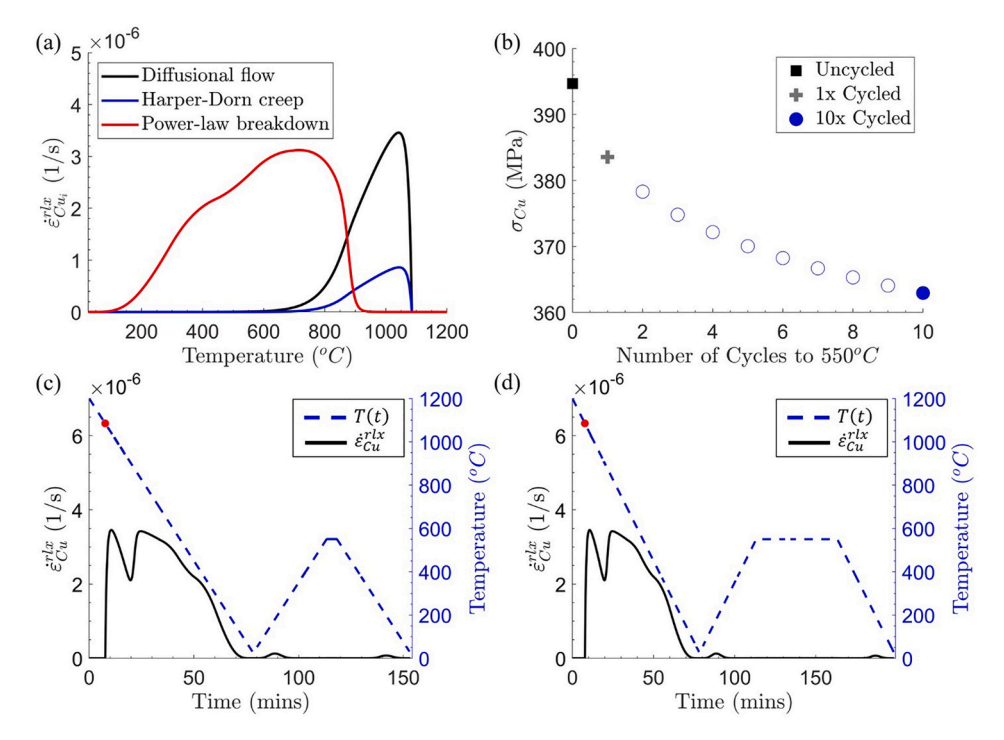


Fig. 3. Modeling results of Cu relaxation evolution. (a) Active creep mechanisms on cooling from infiltration. (b) Relaxation evolution with cyclic heat treatment to $550\,^{\circ}$ C. The effect of hold time at $550\,^{\circ}$ C on relaxation rate for (c) 5-min and (d) 50-min holds with the red dot indicating the melt temperature of Cu – $1085\,^{\circ}$ C. (For interpretation of the references to colour in this figure legend, the reader is referred to the web version of this article.)

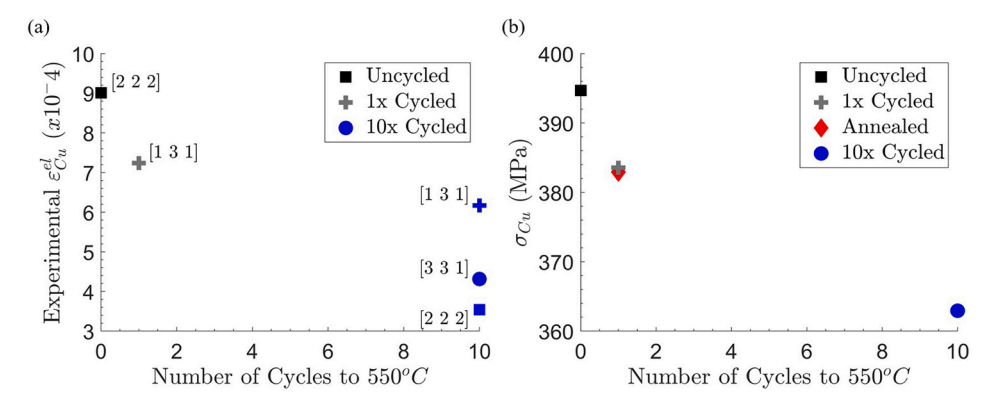


Fig. 4. (a) Experimentally determined elastic strain within identified Cu lattice planes. (b) Model derived homogenized stress in Cu.

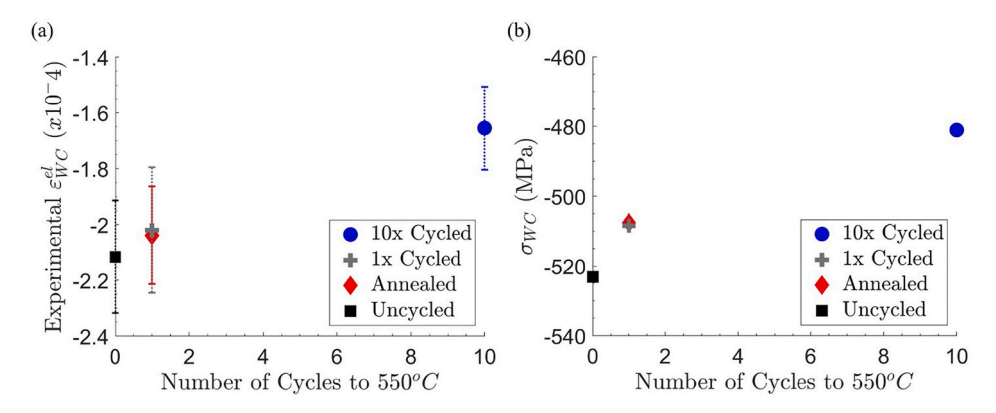


Fig. 5. (a) Experimentally determined elastic strain in WC, with 95% confidence interval. (b) Model derived homogenized stress in WC.

formulation of the model. Fig. 5(a-b) indicates a compressive residual elastic strain/stress state in the WC phase, relaxing with similar trends as the Cu phase, thus satisfying equilibrium. The Annealed and $1\times$ Cycled residual elastic strains in Fig. 5a are within their respective 95% confidence intervals $(1.75\times10^{-5}$ and $2.25\times10^{-5})$, confirming the dependence of relaxation on cycle count, not dwell time, which was consistent with the modeling results.

5. Conclusions

In this work, the residual elastic strain states of both the metallic Cu phase and ceramic WC phase in a co-continuous WC-Cu cermet, exposed to various thermal cycling schedules, were quantified via an analytical homogenized model and experimental energy dispersive X-ray diffraction measurements. Both analysis techniques indicated that structural stability during cooling from processing temperatures, as well as during thermal cycling, was maintained via plasticity within the Cu phase. Additionally, a relaxation mechanism transition from high-temperature diffusional flow to low-temperature dislocation motion, as well as the dependency of stress relaxation on repeated thermal cycling, not annealing dwell time, were identified at the temperature of interest, 550 °C. Lastly, microstructural characterization confirmed a preferentially-oriented Cu phase texture, that was consistent with the dependence of the high-energy X-ray diffraction pattern on rotation angle, generated upon melt-infiltration processing.

From these results, the structural stability of the WC-Cu cermet suggests that this composite could be utilized in certain applications requiring high thermal conductivity and strength as a potential replacement for stainless steel. However, more broadly, the kinetics modeling and X-ray characterization contributions presented are

applicable to a general class of ceramic-metal composites. The illustration of temperature and time-dependent relaxation can be used to tailor processing parameters to minimize the detrimental tensile residual stress in the metallic phase, while the analytical model, with microstructure dependent homogenization, can be used to quantify the residual stress state. Ultimately, further studies are needed to identify the role of residual stress on the susceptibility to thermal-mechanical fatigue of this class of materials.

Declaration of Competing Interest

The authors declare that they have no known competing financial interests or personal relationships that could have appeared to influence the work reported in this paper.

Data availability

Data will be made available on request.

Acknowledgements

MDS would like to thank the National Science Foundation [grant number CMMI 16–51956] for financial support. KHS would like to thank the Department of Energy [grant number DE-EE0008998]. The authors would like to thank Glenn Peterson for assistance during the data acquisition. This work is based upon research conducted at the Center for High Energy X-ray Sciences (CHEXS) which is supported by the National Science Foundation under award DMR-1829070, and at the Materials Solutions Network at CHESS (MSN-C) which is supported by the Air Force Research Laboratory under award FA8650-19-2-5220.

Appendix A

Fig. A.1 compares the full width at half maximum (FWHM) of the WC powder to that of the WC diffraction peaks from the composite. The peak breadth, quantified via the FWHM, is affected by strain inhomogeneity and defects within the diffraction volume. No consistent trend was identified between the powder and composite WC peak breadths, as the peaks corresponding to the [121] and [030] lattice planes had a greater mean FWHM in the composite than the powder, while the [013] lattice plane peak had the opposite. This indicated that the processing and thermal cycling of the composite resulted in few defects in the WC phase. Additionally, the largely spherical agglomerates in the final composite resulted in little local strain variation in the WC phase.

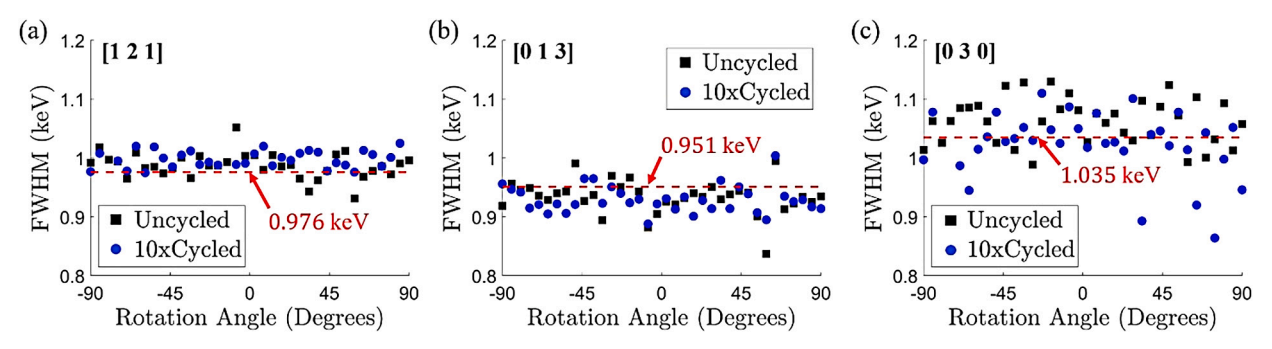


Fig. A.1. FWHM comparison of the WC phase in the WC/Cu composite to the loose WC powder for both the Uncycled and $10 \times$ Cycled samples for diffraction peaks corresponding to the (a) [1 2 1], (b) [0 1 3], and (c) [0 3 0] lattice planes.

Table A.1: Bulk material properties.

Property		Cu		WC	
G	(MPa)	4.21e4 - 16.8(T-20)	[24]	274e3	[25]
$\alpha _{25^{o}C}$	(1/°C)	16.7e-6	[22]	4.4e-6	[23]
$\alpha _{550^{\circ}C}$	(1/°C)	20e-6	[22]	5.6e-6	[23]
ν	(-)	0.34	[26]	0.21	[27]
T_m	(°C)	1083	[28]	2870	[29]

Table A.2: Kinetics properties of Cu.

Property		Value [24]	
γο	(1/s)	1e-6	
ΔF	(J)	3.53e-19	
$\widehat{ au}$	(MPa)	265.23	
$egin{aligned} A_{pl} \ b \end{aligned}$	(-)	7.4e-5	
b	(m)	2.56e-10	
n	(-)	4.8	
D_{ν}	(m^2/s)	$2.5e-5exp\left(\frac{-197e3}{R(T+273)}\right)$	
a_cD_c	(m^4/s)	$2.5\text{e-}5exp\Big(\frac{-197e3}{R(T+273)}\Big)$ $1\text{e-}24exp\Big(\frac{-117e3}{R(T+273)}\Big)$	
α'	(-)	794	
Ω	(m^3)	1.18e-29	
δD_b	(m^3/s)	$5e-15exp\left(\frac{-104e3}{R(T+273)}\right)$	
$A_{H\!D}$	(-)	5e-11	
d	(m)	100e-6	

Table A.3: Cu plastic strain rate models [19,24].

Mechanism	Equation	Variable Definitions
Dislocation glide	$\dot{arepsilon}_{ m dg} = rac{\dot{\gamma}_o}{2\sqrt{3}} { m exp}iggl[rac{-\Delta F}{kT}iggl(1-rac{\sigma}{\sqrt{3}\widehat{ au}}iggr) iggr]$	$\dot{\gamma}_o$ – Reference strain rate ΔF – Activation energy T – Temperature σ – Bulk stress $\hat{\tau}$ – Flow stress at 0 K
Power-law creep	$egin{align} \dot{arepsilon}_{pl} &= rac{A_{pl}D_{eff,pl}\mu b}{2kT}\left(rac{\sigma}{\mu} ight)^n \ D_{eff,pl} &= D_{ u}\left[1 + rac{10a_c}{b^2}\left(rac{\sigma}{\sqrt{3}\mu} ight)^2\!\!D_c ight] onumber \end{aligned}$	A_{pl} – Empirical parameter μ – Shear modulus b – Magnitude of Burgers vector n – Creep exponent (continued on next page)

(continued)

Mechanism	Equation	Variable Definitions
		a_c – Diffusive section of Dislocation core D_c – Dislocation core diffusion coefficient D_v – Lattice diffusion coefficient
Power-law breakdown	$\dot{arepsilon}_{plb} = rac{A_{pl}}{2lpha'^n} rac{D_{eff,pl}\mu b}{kT} igg[ext{sinh} igg(lpha' rac{\sigma}{\mu} igg) igg]^n$	lpha' – Empirical parameter
		Ω – Atomic volume
Diffusional flow	$\dot{arepsilon}_{diff} = rac{7\sigma\Omega}{kTd^2} D_{eff,diff}$	d – Grain size
Diffusional flow		δ – Grain boundary thickness
	$D_{eff,diff} = D_{ m v} \Big[1 + rac{\pi \delta}{d} rac{D_b}{D_{ m v}} \Big]$	D_b – Grain boundary diffusion coefficient
Harper-Dorn creep	$\dot{arepsilon}_{HD} = A_{HD} rac{D_{ u} \mu b}{6kT} \left(rac{\sigma}{\mu} ight)$	A_{HD} – Empirical parameter

References

- N.M. Parikh, M. Humenik, Cermets: II, wettability and microstructure studies in liquid-phase sintering, J. Am. Ceram. Soc. 40 (1957) 315–320, https://doi.org/ 10.1111/j.1151-2916.1957.tb12628.x.
- [2] P.K. Deshpande, J.H. Li, R.Y. Lin, Infrared processed cu composites reinforced with WC particles, Mater. Sci. Eng. A 429 (2006) 58–65, https://doi.org/10.1016/j. msea.2006.04.124.
- [3] M. Caccia, M. Tabandeh-Khorshid, G. Itskos, A.R. Strayer, A.S. Caldwell, S. Pidaparti, S. Singnisai, A.D. Rohskopf, A.M. Schroeder, D. Jarrahbashi, T. Kang, S. Sahoo, N.R. Kadasala, A. Marquez-Rossy, M.H. Anderson, E. Lara-Curzio, D. Ranjan, A. Henry, K.H. Sandhage, Ceramic-metal composites for heat exchangers in concentrated solar power plants, Nature. 562 (2018) 406–409, https://doi.org/10.1038/s41586-018-0593-1.
- [4] D. Zhang, C. Kenel, D.C. Dunand, Microstructure and properties of additively-manufactured WC-Co microlattices and WC-Cu composites, Acta Mater. 221 (2021), https://doi.org/10.1016/j.actamat.2021.117420.
- [5] M. Dias, N. Pinhão, R. Faustino, R.M.S. Martins, A.S. Ramos, M.T. Vieira, J. B. Correia, E. Camacho, F.M. Braz Fernandes, B. Nunes, A. Almeida, U. V. Mardolcar, E. Alves, New WC-Cu composites for the divertor in fusion reactors, J. Nucl. Mater. 521 (2019) 31–37, https://doi.org/10.1016/j.inucmat.2019.04.026.
- [6] W. Ping Shen, Q. Li, K. Chang, Z. Jian Zhou, C. Chun Ge, Manufacturing and testing W/Cu functionally graded material mock-ups for plasma facing components, J. Nucl. Mater. 367-370 (B) (2007) 1449–1452, https://doi.org/10.1016/j. inucmat.2007.04.032.
- [7] J. Chen, C. Zhao, H. Lu, Y. Li, X. Liu, H. Wang, Z. Nie, X. Song, Effects of residual thermal stress on mechanical behavior of cermets with different grain sizes, Acta Mater. 221 (2021), 117428, https://doi.org/10.1016/j.actamat.2021.117428.
- [8] M. Öhman, M. Ekh, F. Larsson, G. Wahnström, Finite element simulations of thermal residual stresses in realistic 3D WC-Co microstructures, Int. J. Refract. Met. Hard Mater. 85 (2019), 105065, https://doi.org/10.1016/j.ijrmhm.2019.105065.
- [9] C.M. Weisbrook, A.D. Krawitz, Thermal residual stress distribution in WC-Ni composites, Mater. Sci. Eng. A 209 (1996) 318–328, https://doi.org/10.1016/ 0921-5093(95)10107-1.
- [10] A. Krawitz, E. Drake, Residual stresses in cemented carbides an overview, Int. J. Refract. Met. Hard Mater. 49 (2015) 27–35, https://doi.org/10.1016/j. ijrmhm.2014.07.018.
- [11] D.P. Gruber, D. Kiefer, R. Rössler, F. Beckmann, M. Tkadletz, T. Klünsner, C. Czettl, J. Keckes, J. Gibmeier, 20 Hz synchrotron X-ray diffraction analysis in laser-pulsed WC-Co hard metal reveals oscillatory stresses and reversible composite plastification, Int. J. Refract. Met. Hard Mater. 82 (2019) 121–128, https://doi.org/10.1016/j.ijrmhm.2019.04.004.
- [12] D. Mari, A.D. Krawitz, J.W. Richardson, W. Benoit, Residual stress in WC-Co measured by neutron diffraction, Mater. Sci. Eng. A 209 (1996) 197–205, https:// doi.org/10.1016/0921-5093(95)10147-0.
- [13] W. Kayser, S. van Kempen, A. Bezold, M. Boin, R. Wimpory, C. Broeckmann, Numerical investigation the of WC re-precipitation impact on the residual stress state in WC20 wt.-%Co hardmetal, Int. J. Refract. Met. Hard Mater. 84 (2019), 105003, https://doi.org/10.1016/j.ijrmhm.2019.105003.
- [14] M. Strantza, R.K. Ganeriwala, B. Clausen, T.Q. Phan, L.E. Levine, D. Pagan, W. E. King, N.E. Hodge, D.W. Brown, Coupled experimental and computational study of residual stresses in additively manufactured Ti-6Al-4V components, Mater. Lett. 231 (2018) 221–224, https://doi.org/10.1016/j.matlet.2018.07.141.
- [15] P. Virtanen, R. Gommers, T.E. Oliphant, M. Haberland, T. Reddy, D. Cournapeau, E. Burovski, P. Peterson, W. Weckesser, J. Bright, S.J. van der Walt, M. Brett,

- J. Wilson, K.J. Millman, N. Mayorov, A.R.J. Nelson, E. Jones, R. Kern, E. Larson, C. J. Carey, İ. Polat, Y. Feng, E.W. Moore, J. VanderPlas, D. Laxalde, J. Perkold,
- R. Cimrman, I. Henriksen, E.A. Quintero, C.R. Harris, A.M. Archibald, A.H. Ribeiro, F. Pedregosa, P. van Mulbregt, A. Vijaykumar, A. Pietro Bardelli, A. Rothberg,
- A. Hilboll, A. Kloeckner, A. Scopatz, A. Lee, A. Rokem, C.N. Woods, C. Fulton,
- C. Masson, C. Häggström, C. Fitzgerald, D.A. Nicholson, D.R. Hagen, D.
- V. Pasechnik, E. Olivetti, E. Martin, E. Wieser, F. Silva, F. Lenders, F. Wilhelm,
- G. Young, G.A. Price, G.L. Ingold, G.E. Allen, G.R. Lee, H. Audren, I. Probst, J.
- P. Dietrich, J. Silterra, J.T. Webber, J. Slavic, J. Nothman, J. Buchner, J. Kulick, J. L. Schönberger, J.V. de Miranda Cardoso, J. Reimer, J. Harrington, J.L.
- C. Rodríguez, J. Nunez-Iglesias, J. Kuczynski, K. Tritz, M. Thoma, M. Newville,
- M. Kümmerer, M. Bolingbroke, M. Tartre, M. Pak, N.J. Smith, N. Nowaczyk,
- N. Shebanov, O. Pavlyk, P.A. Brodtkorb, P. Lee, R.T. McGibbon, R. Feldbauer,
- S. Lewis, S. Tygier, S. Sievert, S. Vigna, S. Peterson, S. More, T. Pudlik, T. Oshima,
- T.J. Pingel, T.P. Robitaille, T. Spura, T.R. Jones, T. Cera, T. Leslie, T. Zito, T. Krauss, U. Upadhyay, Y.O. Halchenko, Y. Vázquez-Baeza, SciPy 1.0:
- fundamental algorithms for scientific computing in Python, Nat. Methods 17 (2020) 261–272, https://doi.org/10.1038/s41592-019-0686-2.
- [16] D.E. Boyce, J.V. Bernier, heXRD: Modular, Open Source Software for the Analysis of High Energy X-Ray Diffraction Data, Lawrence Livermore National Lab (LLNL), Livermore, CA (United States), 2013.
- [17] C. Genzel, I.A. Denks, J. Gibmeier, M. Klaus, G. Wagener, The materials science synchrotron beamline EDDI for energy-dispersive diffraction analysis, Nucl. Inst. Methods Phys. Res. Sec. A: Acceler. Spectrom. Detect. Assoc. Equip. 578 (2007) 23–33, https://doi.org/10.1016/j.nima.2007.05.209.
- [18] A. Kelly, G.W. Groves, P. Kidd, Crystallography and Crystal Defects, Re. ed, Wiley, New York, 2000.
- [19] Y.L. Shen, S. Suresh, Steady-state creep of metal-ceramic multilayered materials, Acta Mater. 44 (1996) 1337–1348, https://doi.org/10.1016/1359-6454(95)
- [20] M. Hoffman, S. Skirl, W. Pompe, J. Rödel, Thermal residual strains and stresses in Al₂O₃/Al composites with interpenetrating networks, Acta Mater. 47 (1999) 565–577, https://doi.org/10.1016/S1359-6454(98)00367-X.
- [21] W. Kreher, W. Pompe, Internal Stresses in Heterogeneous Solids, Akademie-Verlag, Berlin. 1989.
- [22] T.A. Hahn, Thermal expansion of copper from 20 to 800 k standard reference material 736, J. Appl. Phys. 41 (1970) 5096–5101, https://doi.org/10.1063/ 1.1658614
- [23] A.D. Krawitz, D.G. Reichel, R. Hitterman, Thermal expansion of tungsten carbide at low temperature, J. Am. Ceram. Soc. 72 (1989) 515–517, https://doi.org/ 10.1111/j.1151-2916.1989.tb06169.x.
- [24] H.J. Frost, M.F. Ashby, Deformation-Mechanism Maps: The Plasticity and Creep of Metals and Ceramics, 1st ed, Pergamon Press, Oxford, 1982.
- [25] X. Li, X. Zhang, J. Qin, S. Zhang, J. Ning, R. Jing, M. Ma, R. Liu, First-principles calculations of structural stability and mechanical properties of tungsten carbide under high pressure, J. Phys. Chem. Solids 75 (2014) 1234–1239, https://doi.org/ 10.1016/j.jpcs.2014.06.011.
- [26] H.M. Ledbetter, E.R. Naimon, Elastic properties of metals and alloys. II. Copper, J. Phys. Chem. Ref. Data 3 (1974) 897–935, https://doi.org/10.1063/1.3253150.
- [27] R.R. Reeber, K. Wang, Thermophysical properties of alpha tungsten carbide, J. Am. Ceram. Soc. (1999) 129–135, https://doi.org/10.1111/j.1151-2916.1999. tb01732.x.
- [28] H.K. Hieu, N.N. Ha, High pressure melting curves of silver, gold and copper, AIP Adv. 3 (2013), https://doi.org/10.1063/1.4834437.
- [29] A.S. Kurlov, A.I. Gusev, Tungsten Carbides: Structure, Properties and Application in Hardmetals, 2013, https://doi.org/10.1007/978-3-319-00524-9.